Metadata of the chapter that will be visualized online

Chapter Title	Sar Interferometry	
Copyright Year	2011	
Copyright Holder	Springer Science + Business Media B.V.	
Corresponding Author	Family Name	**Furuya**
	Particle	
	Given Name	**Masato**
	Suffix	
	Division	Department of Natural History Sciences
	Organization	Hokkaido University
	Address	N10 W8, Kita-ku, 060-0810, Sapporo, Japan
	Email	furuya@mail.sci.hokudai.ac.jp

S

SAR INTERFEROMETRY

Masato Furuya
Hokkaido University, Sapporo, Japan

Synonyms

Differential InSAR (abbreviated as D-InSAR); Interferometric SAR (abbreviated as InSAR); Radar interferometry; SAR interferometry

Definition

Radar. Acronym standing for Radio Detection and Ranging. A technique to detect any targets and measure the distance to them, based on the round-trip time of microwave (radio wave) pulses between the antenna and the targets.
SAR. Acronym standing for Synthetic Aperture Radar. A technique to image any ground surfaces, using airborne or spaceborne radar sensor. Its high spatial resolution is achieved by collecting numerous return pulses from each target in sight and by effectively synthesizing large antenna size.
InSAR. Acronym standing for Interferometric SAR. A technique to image surface topography and ground displacements, using phase values of two or more SAR images.

Introduction

Crustal deformation data have been traditionally acquired by ground-based geodetic techniques such as leveling, triangulation, and electro-optic distance measurement. More recently, global positioning system (GPS) has become a standard tool for high-precision crustal deformation measurement, and provided us with a wealth of data to study plate tectonics, earthquakes, volcanic activities, and atmospheric and hydrological loading deformation. All these techniques, however, require in situ benchmarks, and thus prevent us from observing inaccessible areas. Interferometric SAR (InSAR) was, therefore, regarded as a surprising and revolutionary technique when Massonnet et al. (1993) first showed an image of the co-seismic deformation associated with the 1992 M7.3 Landers earthquake, because the raw data was completely acquired on a spaceborne sensor. Another big surprise for the community was its incredibly high spatial resolution, which no other geodetic techniques were possible to achieve in practice.

Nowadays, InSAR users have proliferated in a worldwide community and applied to a variety of geophysical problems. A number of excellent and extensive reviews for advanced students and researchers are already published (Bamler and Hartl, 1998; Massonnet and Feigl, 1998; Burgmann et al., 2000; Hanssen, 2001; Pritchard, 2006; Simons and Rosen, 2007; Zhou et al., 2009). I therefore tried to make this article much shorter and more introductory, but it still includes necessary and useful concepts, ranging from the fundamentals of SAR/InSAR imagery to more up-to-date topics.

Fundamentals of SAR imaging and SAR data

SAR satellite flies over at an altitude of hundreds of km, repeating transmission and reception of microwave pulses. The along-track and across-track axes are almost identical to the *azimuth* and *range* axis in the acquired radar image. The area illuminated on the ground is called *swath*, whose width spans roughly 50–100 km in the standard *stripmap* (or *strip*) mode with an incidence angle of 20–50° (Figure 1). While previous SAR applications are mostly derived from the stripmap mode, another imaging mode, *ScanSAR*, is also promising because it covers much wider swath width, 300–500 km, by illuminating multiple swaths at the expense of reducing the resolution. ScanSAR is useful for imaging long-wavelength signals

Harsh K. Gupta (ed.), *Encyclopedia of Solid Earth Geophysics*, DOI 10.1007/978-90-481-8702-7,

associated with, for instance, a magnitude-8-class earthquake (Motagh et al., 2008).

Although it was not strictly necessary, satellite-based SAR system has been often placed on a sun-synchronous and near-polar orbit with an inclination angle of slightly greater than 90°. When the satellite moves to the north (south), we call it is in *ascending* (*descending*) orbit.

The raw data acquired on SAR sensor are impossible to visually interpret, and require a bit involved processing algorithms; those algorithms are detailed in a couple of text books (e.g., Curlander and McDonough, 1991; Cumming and Wong, 2005). The first interpretable SAR image is a single-look-complex (SLC) image, whose important difference from other optical images is that each pixel consists of a complex (real and imaginary) value, i.e., amplitude and phase. This is because the waveform of each repeated pulse is precisely controlled to be identical, and hence the received pulse provides us with not only a scattering (reflection) *intensity* but also a *phase*. The phase data do contain the geometric information from the antenna to the ground targets, and are fully exploited in generating InSAR image as discussed later. However, the phase image itself is usually not as useful as the intensity image because it is again impossible to visually interpret the physical meaning. Meanwhile, the intensity image is often useful and derived from a square-root magnitude of SLC data with spatial averaging called *multi-looking*. By single-look, it means the finest spatial resolution for both range and azimuth axis. In the standard stripmap mode, the range and azimuth resolutions are derived as,

$$\Delta r = \frac{c}{2B}, \quad and \quad \Delta a = \frac{L}{2}, \tag{1}$$

respectively; the c, B, and L are the speed of light, the frequency bandwidth of the microwave pulse, and the antenna length along azimuth axis, respectively (Curlander and McDonough, 1991; Cumming and Wong, 2005). The waveform of each microwave pulse is called *chirp signal*, whose instantaneous frequency linearly changes by as much as the frequency bandwidth B over the duration of each pulse. It should be noted that the spatial resolution depends neither on the sensor altitude nor the carrier frequency of microwave. Intensity images are often shown in gray scale images, in which strongly (weakly) reflected objects/areas are usually colored as bright (dark). Although they simply look like black-and-white photographs, we should keep in mind that they could be acquired regardless of weather and time because SAR is actively transmitting and receiving microwaves. Also, intensity images are indispensable for high-precision image matching prior to a generation of InSAR image.

Fundamental principles of InSAR

Interferometric SAR (InSAR) is a technique to generate a digital elevation model (DEM) or a ground displacement image from a *pair* of SLC images. The term *interferogram* is often used to represent InSAR image. We can understand the principle of InSAR, recalling the classical Young's experiment that is known to be a proof of the wave characteristics of the light (Ghilia and Pritt, 1998). Two coherent waves out of the slits will generate "stripes" on the wall, called interference *fringe* (Figure 2a). We can simulate the fringe if we know the separation of the slits, the distance from each slit to the wall, and the wavelength of the coherent wave. Depending on the path difference, the two coherent waves are in-phase or out-of-phase when they reach the screen. Namely, the difference of the phases generates the interference fringe. We may regard the imaging geometry of InSAR as the 3-D Young's experiment (Figure 2b). The repeat orbit tracks, the ground surface, and the microwave correspond to the double slits, the screen, and the coherent wave, respectively. Once we get two SLC images, we can generate an initial interferogram, multiplying one SLC image with the complex conjugate of the other SLC image. We then observe similar fringes in the initial interferogram as illustrated in Figure 2b, which is literally a map of the difference of two SLC phases. For descriptive purposes, the former SLC image is often denoted as *master*, and the latter SLC image is called *slave*. At this moment, the slave image must be precisely co-registered (or matched) to the master image (Figure 3); we will come back to this *image co-registration* (or *image matching*) procedure later on.

While Figure 2b shows an initial interferogram over flat areas with parallel orbits, the fringe will appear undulated if the areas are not flat. The fringe over flat areas is called *flat Earth fringe* (or, *orbital fringe*), and can be precisely simulated from the pair of orbit data. If we subtract the flat Earth fringes from the initial interferogram, we can extract *topographic fringe* that can be used to generate DEM. The Shuttle Radar Topography Mission (SRTM) was carried out along this idea in 2001, and generated 3-s resolution DEM over +/− 60° latitudes (Farr et al., 2007). In the case of SRTM, they carried two SAR antennas on the same platform, and thus were able to generate DEM without repeating the previous orbit track. In contrast, all the present SAR satellite systems carry only one antenna with a repeat-pass period of several weeks, which are 11 days for TerraSAR-X, 16 days for COSMO-SkyMed, 24 days for Radarsat-1/2, 35 days for Envisat, and 46 days for ALOS. Therefore, if ground surface undergoes significant deformation during the repeat orbit cycles due, for instance, to earthquake and volcanic eruption, the interferogram will include *deformation fringe* as well. To extract deformation fringe, we must take out both orbital fringe and topographic fringe, which can be simulated from satellite orbit data and DEM. The deformation fringes represent slant range changes along the radar line-of-sight (LOS), and thus projections of the 3-D displacement vector on the ground along the unitary vectors toward the radar LOS (Figure 4). The range changes should be interpreted as relative displacements to the reference point(s) inside each interferogram. Depending on literatures, they denote differential interferometric SAR

(D-InSAR) when the technique is used to detect deformation signals. Recently, however, the term InSAR is often and simply used to represent D-InSAR.

Even if no significant ground displacements take place during the repeat-pass period, however, we usually encounter other non-negligible fringes due to the spatial heterogeneities in the propagation delay of microwaves through the atmosphere, the errors in satellite orbit data, and those in DEM. Because these fringes limit the precision and accuracy of SAR-based crustal deformation measurement, a couple of correction approaches have been proposed. More advanced time-series analysis techniques have also been developed to overcome the issues, which will be introduced in the last section.

InSAR processing

Image registration (Matching): Before we get an initial interferogram, we must register (or, match) each imaged target in one SLC image to the same target in the other SLC image with a sub-pixel level accuracy, because any ground objects do not usually locate at the same pixel coordinates in each SLC image. This pre-processing is called *image registration* (or *image matching*) and prerequisite to be performed prior to generating an initial interferogram. Although a simple polynomial transformation between the range and azimuth coordinates of two SLC images is sufficient in most cases, we need to take into account the effects of 3-D topography when the terrain surface is rugged to eliminate a stereoscopic effect (Michel et al., 1999).

When large ground displacements on the order of meters or more take place locally, and if we correct for the long-wavelength image distortion using the polynomial transformation, we can detect and quantify those localized displacements as a by-product of image registration without viewing InSAR image (Figure 3; Tobita et al., 2001a). This approach to detect large displacements is called *pixel offset* or *feature tracking* technique, and has been applied to earthquakes, volcanic eruptions, and glacier movements. The advantages of pixel-offset data are twofolds. First, pixel-offset data can quantify large displacements even in such areas that completely loses interferometric coherence, where InSAR data cannot be unwrapped; we describe *coherence* and *unwrapping* later below. Secondly, in contrast to InSAR data, pixel-offset data provide us with not only range offset but also azimuth offset component. While the range offset has the same sensitivity to the 3-D displacement vector as InSAR data (Figure 4), the azimuth offset is a projection of the displacement vector onto the unitary vector perpendicular to the LOS. Hence, the azimuth offset data are complementary to the range offset or InSAR data. Taking advantage of this property, Fialko et al. (2001) derived a full 3-D displacement map for the 1999 M7.1 Hector Mine earthquake, combining the InSAR data from both ascending and descending track with the azimuth offset data. Using pixel-offset data from both descending and ascending track, Tobita et al. (2001a,b) inferred a 3-D displacement map associated with the 2,000 eruption episode at Usu volcano.

Interferometric phase and its relation to geometry: Suppose we have two co-registered SLC images, E_1 and E_2, acquired from different ranges r_1 and r_2:

$$E_1 = e^{j\phi_{Scatter}} e^{-\frac{4\pi r_1}{\lambda}} \tag{2a}$$

$$E_2 = e^{j\phi_{Scatter}} e^{-\frac{4\pi r_2}{\lambda}} \tag{2b}$$

Here we assume that the reflection magnitude and scattering phase are constant during the data acquisition time. Then, the interferometric phase ϕ is derived as

$$E_1 E_2^* = e^{-\frac{4\pi(r_1 - r_2)}{\lambda}} \tag{3}$$

or

$$\phi = \frac{4\pi}{\lambda}(r_1 - r_2) \tag{4}$$

The last one is the fundamental equation for InSAR, which describes "unwrapped" phase in the initial interferogram. The actual phase in the initial interferogram is "wrapped" into an interval $[-\pi, \pi]$, and thus has ambiguities of $2\pi N$; N is integer. In order to quantify the ground displacement along radar LOS, we have to perform 2-D *phase unwrapping* on the interferogram, which is not necessarily straightforward (Bamler and Hartl, 1998; Ghilia and Pritt, 1998). While the interferometric phase is strictly a phase "difference" of two SLC phases, it is conventional to simply call phase. The factor 4 is to take into account the round-trip distances.

Figure 5 is a cross section that is perpendicular to the satellite repeat tracks and passes through the Earth's center, and shows a geometry of InSAR data acquisition. The spatial separation of the repeating orbits is termed *baseline* (or *spatial baseline*), B; the temporal separation of data acquisition is sometimes called *temporal baseline*. Because the baseline B is usually much shorter than the ground range distance R, a parallel ray approximation holds (Zebker et al., 1994) and the fundamental Equation 4 can be approximated as follows:

$$\phi = \frac{4\pi}{\lambda}(r_1 - r_2) \approx -\frac{4\pi}{\lambda} B_{//} = B\,Sin(\theta - \alpha), \tag{5}$$

where θ and α are defined in Figure 5, and $B_{//}$ (or B_{para}) is a baseline component parallel to the radar LOS. The angle θ is called *off-nadir angle*, and is identical to incidence angle if the Earth's curvature is negligible. The other baseline component $B_{\perp}$ (or B_{perp}) is perpendicular to radar LOS and gives us an important criterion for successful InSAR processing as we discuss below.

Decorrelation (Coherence): In the actual InSAR data processing, we do not necessarily get clear fringes over the entire area. Depending on the data pairs and places, it is not uncommon that no fringes are observed. To detect

clear fringes, the reflected waves received at master and slave acquisitions must be more or less correlated to each other. The degree of correlation is quantified as *coherence*, and there are two independent decorrelation sources.

The first source of decorrelation originates in the imaging geometry. As Figure 6 indicates, we observed higher (fewer) fringe density as becomes longer (shorter); imagine the case of zero baseline length. The fringe density can be derived from the gradient of phase (Equation 5) along the range axis:

$$\frac{\partial \phi}{\partial R} = -\frac{4\pi B_\perp}{\lambda R \tan\theta} + \frac{4\pi B_\perp}{\lambda (r_e + H)\sin\theta} \approx -\frac{4\pi B_\perp}{\lambda R \tan\theta}. \quad (6)$$

Namely, the fringe density is proportional to the perpendicular baseline $B_\perp$, and inversely proportional to the wavelength λ; see Simons and Rosen (2007) for the case with topography. If the fringe density becomes too high to be counted within a range resolution of SAR image, we will not be able to identify any orbital fringes. This type of decorrelation is termed *baseline decorrelation* (or *spatial decorrelation*). The *critical baseline* is given as such a perpendicular baseline that gives a phase gradient 2π over the range resolution Δr;

$$B_\perp^c = \frac{\lambda R \tan\theta}{2\Delta r}.$$

For a typical value of ALOS/PALSAR with $\lambda = 23(cm)$, $R = 870(km)$, $\theta = 34^\circ$, $\Delta r = 5(m)$, the critical baseline becomes $B_\perp^c = 135,000(m)$, which gives an upper limit of $B_\perp$. However, we practically prefer much shorter $B_\perp$, generally less than ~2,000 m for ALOS/PALSAR, because in more realistic situations the effect of topography also comes in. The longer the $B_\perp$, the more sensitive to rugged terrain as Figure 6 indicates. To eliminate topographic fringes, we need more accurate and higher resolution DEM if the $B_\perp$ becomes longer. Massonnet et al. (1996) proposed an alternative approach that could effectively reduce the $B_\perp$ by a combination of integer multiplied (wrapped) interferograms. For instance, if one interferogram with perpendicular baseline of 300 m is combined with the other interferogram with perpendicular baseline of 290 m with factors 1 and -1, the effective perpendicular baseline becomes 10 m. The scaling operation, however, also scales the amount of noise, and thus the approach is limited to small integer numbers.

The second type of decorrelation is termed *temporal decorrelation*, which is related to the scattering phase in the Equation 2a, and originates in how the microwave pulses interact with the physical objects near the ground. We often encounter the temporal decorrelation problem over vegetated areas with C-band (shorter-wavelength) SAR data and/or snow-covered areas; see Figure 7. It should be recalled that each pixel value in SLC image is a superposition of all the reflected microwaves from all scatterers inside each resolution cell (~5 × ~10 m). Short-wavelength microwave pulses tend to be reflected on the vegetation canopies before reaching the ground surface, and their random motion will result in different scattering phases at different acquisition time, causing temporal decorrelation. On the contrary, long-wavelength microwave pulses can more easily reach the ground, which does not move as rapidly as vegetations, and thus the resulting scattering phases will be also stable over time. Besides the selection of wavelength, the polarization of microwave is also essential for better coherence over time. While, most presently, operated satellite-SAR sensors are capable of multi-polarization modes, it was shown that HH-polarization gives better coherence than VV-polarization (Cloude and Papathanassiou, 1998). This is because the HH-polarized pulses can more easily penetrate through vegetations.

Outlook for InSAR geodesy

Limitations of present InSAR: Although it has a potential to detect tens of km-scale or even larger-scale secular deformation signals on the order of mm/year, InSAR technique has been most successfully applied to detection of spatially localized signals on the order of centimeters or more, such as those associated with earthquakes, volcanic eruptions, and ground subsidence. This is because the artifacts due to inaccurate satellite orbit data and/or microwave propagation delays (advances) in the troposphere (ionosphere) can mask small-amplitude, long-wavelength deformation signals that are similar in both their amplitude and the spatial scale.

Although high-precision orbit data are indispensable to correct for the orbital fringes in the initial interferograms, their errors even on the order of 10 cm or less will generate non-negligible long-wavelength artifacts, which usually look like curved surfaces in the entire interferogram (e.g., Hanssen, 2001). Conventionally, they are fitted with low-order polynomials and simply taken out unless any sort of stacking or time-series analysis discussed below is applied. While this procedure works to eliminate the artifacts due to orbit errors, it will also take out any long-wavelength geophysically interesting signals such as the inter-seismic, post-seismic, ocean tidal loading, solid-Earth tide, and post-glacial rebound signals. Alternatively, if the ground control points (GCP) are available, where the precision ground deformation data are available, we can reestimate the baseline, based on those GCP data (e.g., Rosen et al., 1996), but such data are often unavailable in remote areas.

One approach to correct for the tropospheric delay signals is to employ the other independent estimates derived from either the GPS-based tropospheric delay estimates (e.g., Onn and Zebker, 2006) or the output results from high-resolution numerical weather model (e.g., Foster et al., 2006). These so-called calibration approaches are, however, not easily applicable. The dense ground-based GPS network is limited to a few areas in the world. Also, high-resolution numerical weather model still needs significant computational resources.

Besides the tropospheric delay problem, the effects of ionosphere on both interferograms and pixel-offset images were clearly recognized in the results of the 2008 Wenchuan earthquake (Mw7.9), China, derived from ALOS/PALSAR (Kobayashi et al., 2009; Raucoules and de Michele, 2010), although they were pointed out in polar region many years ago (e.g., Matter and Gray, 2002). It is well known that the lower the carrier frequency is, the more significant the ionospheric dispersion impacts on the propagation delay. Thus, in many of the previous applications of C-band SAR data, the effects of ionosphere could have been neglected. While GPS also employs L-band, the high-precision GPS geodetic survey corrects for the ionospheric effect with the use of dual frequency, L1 and L2, observation data. In contrast, PALSAR is a single frequency SAR sensor and incapable of the standard ionosphere-correction approach. Empirically, however, we will encounter the ionospheric signals more frequently in the ascending data acquired in the local nighttime than in the descending data acquired in the local daytime. We also recall that the JERS, the other L-band SAR operated during 1992–1998, did not reveal any significant ionospheric signals at least in mid-latitude regions, and that most of the JERS data were acquired in the descending track. Besides the latitude, the effects of ionosphere on SAR image might, therefore, significantly depend on the data acquisition time. Like the tropospheric effects, detailed studies of ionospheric impacts on the SAR data are also currently underway.

A simple approach to eliminate those noises is *stacking*, in which several interferograms are stacked to isolate small-amplitude signals, because those noises can be regarded as temporally random, whereas the deformation signals are spatially persistent. Two important prerequisites for successful stacking are: (1) the data acquisition dates of those interferograms should not be overlapped, in order not to enhance the noises of any particular acquisition date(s), and (2) each temporal baseline should be as long as possible so that each interferogram can include as much deformation signals as possible. In reality, it is not easy to gather many independent interferograms that have desirably long temporal baselines because the available data often encounter the spatial and temporal decorrelation. Also, the simple stacking approach inherently assumes temporally linear evolution in the ground deformation, preventing us from deriving time-series data.

Time-Series Analysis: Ferretti et al. (2000, 2001) proposed a new analysis technique called *Permanent Scatterer InSAR* (*PS-InSAR*), in which they take advantage of even such data pairs whose spatial baselines are longer than the critical values. Thereby, they could expand the temporal coverage, and thus could estimate the long-term deformation signals on the order of mm/year. Key idea of PS-InSAR is to pick up only such pixels that will exhibit long-term coherence due to the existence of corner-reflector-like targets, which Ferretti et al. called "permanent scatterers." Based on those pixels alone, they generate a stack of differential interferograms, using available DEM and orbit data. The phase values include not only deformation signals, but also such topographic signals that were not initially taken into account, because the longer spatial baseline pairs are so sensitive to the topography that the available DEM could not account for. In PS-InSAR and its variants (Werner et al., 2003; Hooper et al., 2004), they fit the differential interferogram stack to a phase model that describes not only temporal evolution of deformation but also corrections to the available DEM. Deviations from the phase model can be filtered into either non-linear deformation or atmospheric signals because the former signals are correlated and thus low-pass filtered along temporal axis, while the latter signals are temporally random; the orbit data must be assumed to be correct. A known limitation of PS-InSAR is its rather lower sampling density over non-urban areas. However, despite a lack of man-made objects, Furuya et al. (2007) succeeded in detecting active salt tectonic motion, applying a similar technique to Canyonlands National Park, Utah, presumably because the area was non-vegetated and the exposed surface rocks behaved like corner-reflector-like targets.

Another time-series analysis approach was devised and known as small baseline subset (*SBAS*) algorithm (Berardino et al., 2002). Key idea of the SBAS algorithm is *least-squares inversion* of unknown deformation at each SAR data acquisition epoch, based on the available unwrapped differential interferograms (e.g., Lundgren et al., 2001; Schmidt and Burgmann, 2003). Using small baseline interferometric pairs, the SBAS approach is free from spatial decorrelation and allows us to take advantage of the fine spatial resolution of InSAR data. If the number of interferograms is greater than or equal to the number of SAR acquisitions, the inversion problem becomes an over-determined or well-determined problem, and can be easily solved in a least-squares approach. It is uncommon, however, that all the available interferometric pairs have short baselines, and accordingly the temporal sampling rate will decrease. Berardino et al. (2002) proposed to employ several groups of "small baseline subset" to overcome the lower temporal resolution issue, and solved the rank-deficient problem with the use of singular value decomposition (SVD) technique. The SVD gives the minimum-norm least-squares solution, which is equivalent to minimizing the estimated velocities at any time intervals.

Time-series analysis of SAR data is a promising technique, but almost all previous analyses are based on the C-band ERS1/2 and Envisat data, because not only more-than-decade-long data but also high-precision, well-controlled satellite orbits are available for these satellites. As noted before, not all geophysically interesting phenomena could be detected by C-band and shorter-wavelength SAR data. If the L-band ALOS/PALSAR data are archived for a much longer time, and if the follow-on ALOS-2 and the DESDynI are launched as scheduled, the time-series analysis of SAR data will become feasible even in areas that have never been monitored before. The time-series analysis with ScanSAR data should also be

possible. Long-term continuous monitoring with L-band SAR will provide us with more opportunities for new discoveries.

Bibliography

Bamler, R., and Hartl, P., 1998. Synthetic aperture radar interferometry. *Inverse Problems*, **14**, R1.

Berardino, P., Fornaro, G., Lanari, R., and Sansosti, E., 2002. A new algorithm for surface deformation monitoring based on small baseline differential SAR interferograms. *IEEE Transactions on Geoscience Remote Sensing*, **40**, 2375.

Burgmann, R., Rosen, P. A., and Fielding, E. J., 2000. Synthetic aperture radar interferometry to measure Earth's surface topography and its deformation. *Annual Review of Earth and Planetary Sciences*, **28**, 169.

Cloude, S. R., and Papathanassiou, K. P., 1998. Polarimetric SAR Interferometry. *IEEE Transactions on Geoscience Remote Sensing*, **36**, 1551.

Cumming, I. G., and Wong, F. H., 2005. *Digital Processing of Synthetic Aperture Radar Data: Algorithm and Implementation*. Boston: Artech House.

Curlander, J. C., and McDonough, R. N., 1991. *Synthetic Aperture Radar: Systems and Signal Processing*. New York: Wiley interscience.

Farr, T. G., et al., 2007. The shuttle radar topography mission. *Reviews of Geophysics*, **45**, RG2004.

Ferretti, A., Prati, C., and Rocca, F., 2000. Nonlinear subsidence rate estimation using permanent scatterers in differential SAR interferometry. *IEEE Transactions on Geoscience and Remote Sensing*, **38**, 2202.

Ferretti, A., Prati, C., and Rocca, F., 2001. Permanent scatterers in SAR interferometry. *IEEE Transactions on Geoscience and Remote Sensing*, **39**, 8.

Fialko, Y., Simons, M., and Agnew, D., 2001. The complete (3-D) surface displacement field in the epicentral area of the 1999 Mw7.1 hector mine earthquake, California, from space geodetic observations. *Geophysical Research Letters*, **28**, 3063.

Foster, J., Brooks, B., Cherubini, T., Shacat, C., Businger, S., and Werner, C. L., 2006. Mitigating atmospheric noise for InSAR using a high resolution weather model. *Geophysical Research Letters*, **33**, L16304.

Furuya, M., Mueller, K., and Wahr, J., 2007. Active salt tectonics in the Needles District, Canyonlands (Utah) as detected by interferometric synthetic aperture radar and point target analysis: 1992–2002. *Journal of Geophysical Research*, **112**, B06418.

Ghilia, D. C., and Pritt, M. D., 1998. *Two Dimensional Phase Unwrapping: Theory, Algorithms, and Software*. New York: Wiley.

Hanssen, R. F., 2001. *Radar Interferometry: Data Interpretation and Error Analysis*. Dordrecht: Kluwer.

Hooper, A., Zebker, H., Segall, P., and Kempes, B., 2004. A new method for measuring deformation on volcanos and other natural terrains using InSAR persistent scatterers. *Geophysical Research Letters*, **31**, L23611.

Kobayashi, T., Takada, Y., Furuya, M., and Murakami, M., 2009. Location and types of ruptures involved in the 2008 Sichuan Earthquake inferred from SAR image matching. *Geophysical Research Letters*, **36**, L07302.

Lundgren, P., Usai, S., Sansosti, E., Lanari, R., Tesauro, M., Fornaro, G., and Berardino, P., 2001. Modeling surface deformation observed with synthetic aperture radar interferometry at Campi Flegrei caldera. *Journal of Geophysical Research*, **106** (B9), 19355.

Massonnet, D., and Feigl, K. L., 1998. Radar interferometry and its application to changes in the earth's surface. *Reviews of Geophysics*, **36**, 331.

Massonnet, D., Rossi, M., Carmona, C., Adragna, F., Peltzer, G., Feigl, K., and Raboute, T., 1993. The displacement field of the Landers earthquake mapped by radar interferometry. *Nature*, **364**, 138.

Massonnet, D., Vadon, H., and Rossi, M., 1996. Reduction of the need for phase unwrapping in radar interferometry. *IEEE Transactions on Geoscience and Remote Sensing*, **34**, 489.

Matter, K. E., and Gray, A. L., 2002. Reducing ionospheric electron density errors in satellite radar interferometry applications. *Canadian Journal of Remote Sensing*, **28**, 583.

Michel, R., Avouac, J.-P., and Taboury, J., 1999. Measuring ground displacements from SAR amplitude images: application to the landers earthquake. *Geophysical Research Letters*, **26**, 875.

Motagh, M., Wang, R., Walter, T. R., Bürgmann, R., Fielding, E., Anderssohn, J., and Zschau, J., 2008. Coseismic slip model of the 2007 august pisco earthquake (Peru) as constrained by wide swath radar observations. *Geophysical Journal International*, **174**, 842.

Onn, F., and Zebker, H. A., 2006. Correction for interferometric synthetic aperture radar atmospheric phase artifacts using time series of zenith wet delay observations from a GPS network. *Journal of Geophysical Research*, **111**, B09102.

Pritchard, M. E., 2006. InSAR, a tool for measuring Earth's surface deformation. *Physics Today*, **59**(7), 68.

Raucoules, D., and de Michele, M., 2010. Assessing Ionospheric Influence on L-Band SAR Data: Implications on Coseismic Displacement Measurements of the 2008 Sichuan Earthquake. *IEEE Geoscience Remote Sensing Letters*, **7**, 286.

Rosen, P. A., Hensley, S., Zebker, H. A., Webb, F. H., and Fielding, E. J., 1996. Surface deformation and coherence measurements of Kilauea volcano, Hawaii, from SIR-C radar interferometry. *Journal of Geophysical Research*, **101**(E10), 23109.

Schmidt, D. A., and Burgmann, R., 2003. Time-dependent land uplift and subsidence in the Santa Clara valley, California, from a large interferometric synthetic aperture radar data set. *Journal of Geophysical Research*, **108**(B9), 2416.

Simons, M., and Rosen, P. A., 2007. Interferometric synthetic aperture radar geodesy. In Herring, T. A. (ed.), *Treatise on Geophysics*. New York: Elsevier, Vol. 3, pp. 391–446.

Tobita, M., Murakami, M., Nakagawa, H., Yarai, H., and Fujiwara, S., 2001a. Two-dimensional field of three-dimensional components of deformations and velocities, and volume change around Usu Volcano associated with the 2000 eruption by matching of SAR images (in Japanese). *Journal of Geographical Survey Institute*, **95**, 37.

Tobita, M., Murakami, M., Nakagawa, H., Yarai, H., Fujiwara, S., and Rosen, P. A., 2001b. 3D surface deformation of the 2000 Usu Eruption measured by matching of SAR images. *Geophysical Research Letters*, **28**, 4291.

Werner, C. L., Wegmuller, U., Strozzi, T., and Wiesmann, A., 2003. Interferometric point target analysis for deformation mapping, paper presented at IGARSS'03, Toulouse: Geoscience Remote Sensing Society.

Zebker, H. A., Rosen, P. A., Goldstein, R. M., Gabriel, A., and Werner, C. L., 1994. On the derivation of coseismic displacement fields using differential radar interferometry: The Landers earthquake. *Journal of Geophysical Research*, **99**(B10), 19617–19634.

Zhou, X. B., Chang, N. B., and Li, S. S., 2009. Applications of SAR Interferometry in Earth and Environmental Science Research. *Sensors*, **9**, 1876.

Cross-references

Earthquake and Crustal Deformation
Earthquake Rupture
Earthquake Source, Theory
Geodesy, Ground Positioning and Leveling
GPS –Tectonic Geodesy-
Inverse Theory, Global Optimization
Inverse Theory, Monte Carlo Method
Inverse Theory, Singular Value Decomposition
Inverse Theory: Linear
Remote Sensing and GIS Techniques for Tectonic Studies
Remote Sensing, Applications to Geophysics
Slow Earthquakes

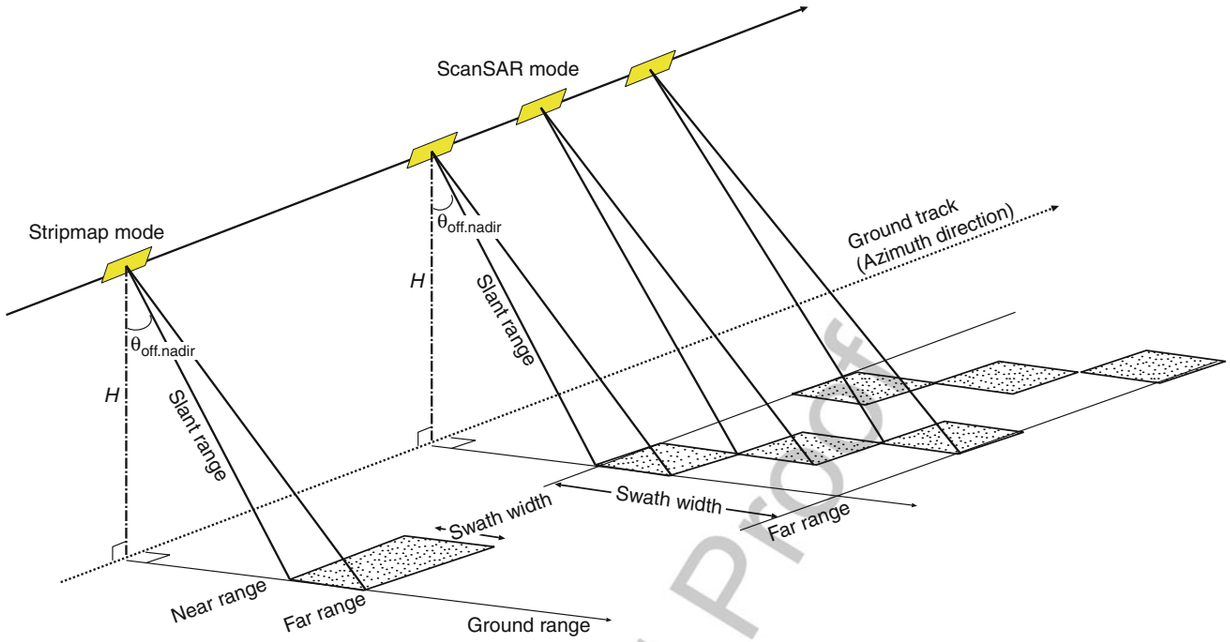

Sar Interferometry, Figure 1 Geometry of SAR imaging. SAR sensor transmits microwave pulses in slant range direction, and receives their reflected pulses. While stripmap mode achieves high spatial resolution with a fixed off-nadir angle, ScanSAR mode achieves wider imaged area (swath) with multiple off-nadir angles at the expense of the resolution.

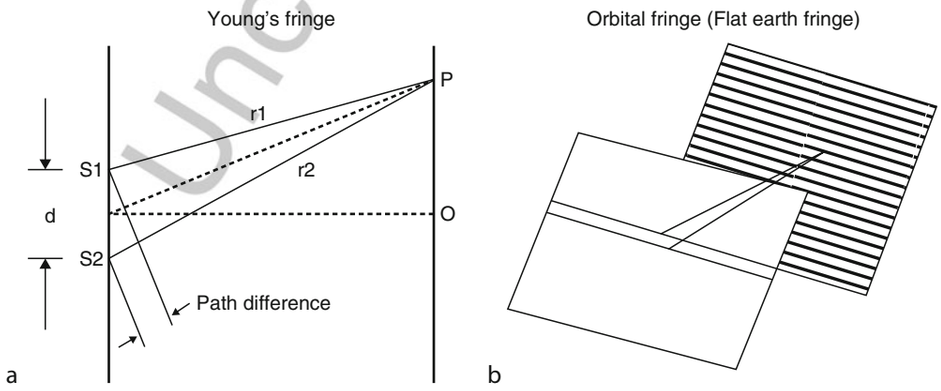

Sar Interferometry, Figure 2 (**a**) Geometry of the Young's experiment. Depending on the path difference, the two coherent waves from the slit, S1 and S2, are in-phase or out-of-phase on the screen, and interference fringes are observed on the right screen. (**b**) Orbital fringe (flat earth fringe) can be regarded as a 3-D analogue of the Young's experiment.

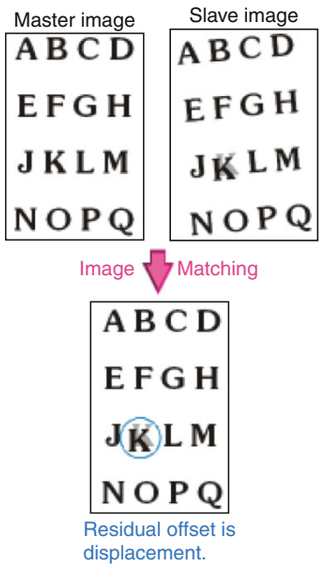

Sar Interferometry, Figure 3 Image registration (matching) of the master and slave images prior to interferogram generation, and the principle of pixel-offset technique to derive large displacements. While long-wavelength distortion can be corrected, localized huge displacement remains as residual offset. Courtesy of Tobita et al. (2001a).

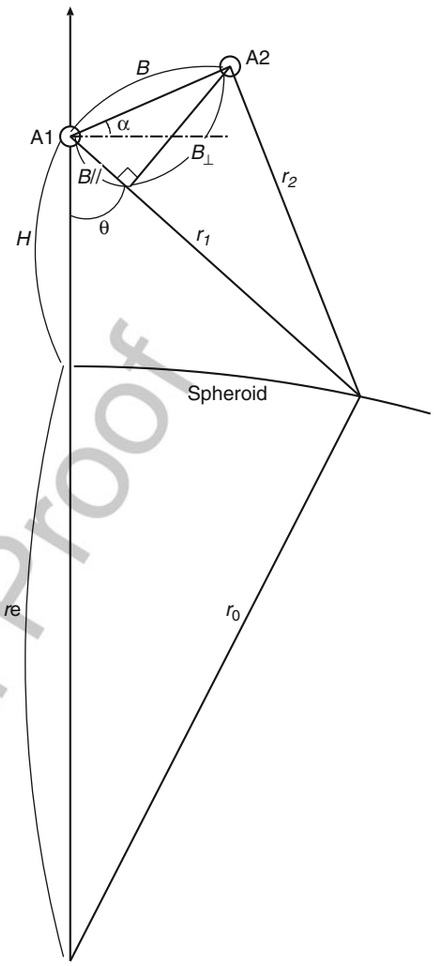

Sar Interferometry, Figure 5 Geometry of InSAR data acquisition and its relation to the baseline. The A1 and A2 are the satellite's repeat orbits, and the spatial distance between the A1 and A2 is the baseline B. The initial InSAR phase is proportional to the difference between the ranges, r_1 and r_2, and hence the *Bpara* (eq. 5). The fringe rate (density) along the range axis is proportional to the *Bperp* (eq. 6).

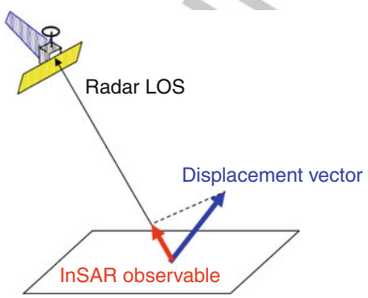

Sar Interferometry, Figure 4 InSAR observable is a projection of the displacement vector along the radar line-of-sight (LOS) direction.

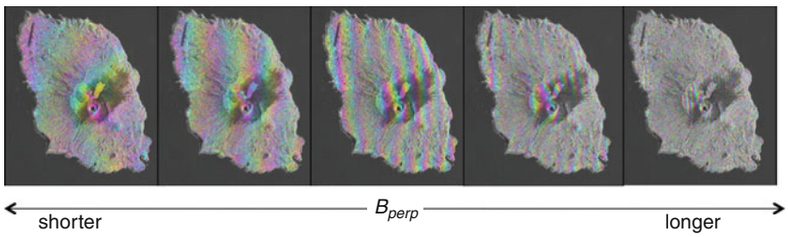

Sar Interferometry, Figure 6 The fringe rate (density) depends on the *Bperp*; see eq (6). The shorter the *Bperp*, the fewer the observed fringes, and thus better to detect deformation signals. In order words, there is a limit in the *Bperp* over which we cannot count the number of fringes. The InSAR image is based on JERS data over Izu-Oshima volcano island, Japan. Original SAR data is copyrighted by JAXA and MITI, Japan.

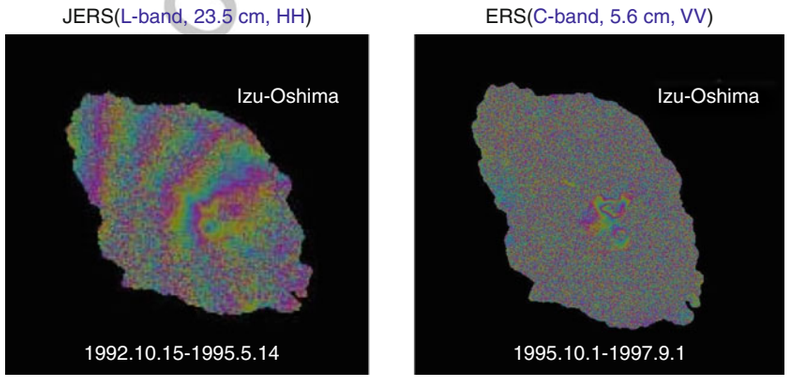

Sar Interferometry, Figure 7 Comparison of two interferograms at Izu-Osima volcano, derived from (left) L-band HH JERS data and (right) C-band VV ERS data. While clear fringes are observed to the left even with 2.5 years temporal baseline, we can recognize the fringes only around the caldera that are covered with few vegetations.